PCCP

View Online
Dynamic Article Links

Cite this: DOI: 10.1039/c1cp20188c

www.rsc.org/pccp

PAPER

Iron oxyhydroxide nanoparticles formed by forced hydrolysis: dependence of phase composition on solution concentration

Dong Fu,[a] Peter G. Keech,[a] Xueliang Sun[b] and J. Clara Wren*[a]

Received 21st January 2011, Accepted 22nd August 2011
DOI: 10.1039/c1cp20188c

Nanoparticles of single-phase lepidocrocite (γ-FeOOH) and goethite (α-FeOOH) have been synthesized by forced hydrolysis of ferric nitrate with no other additives, and the particles have been characterized by XRD, FT-IR and TEM. At low $Fe(NO_3)_3$ concentrations the hydrolysis product is predominantly γ-FeOOH, while at high concentrations it is α-FeOOH. These particles are nanometers in size and fall within narrow particle size distributions. The dependence of the oxyhydoxide phase on ferric nitrate concentration is attributed to two thermodynamic factors, the enthalpy of formation and the surface enthalpy of hydration at the oxide-water interface (which is a function of surface area). Two potential mechanisms for the phase-specific growth are proposed that explain the solution concentration dependence of the phase formed. Three other common nanoscale particles (α-Fe_2O_3, Fe_3O_4 and γ-Fe_2O_3) have also been prepared by relatively simple thermal/chemical treatment of the γ-FeOOH nanoparticles.

1. Introduction

Nanometer-sized particles have many applications owing to the physical and chemical properties that arise from their high surface-to-volume ratios.[1–3] Specifically, iron oxide-based nanoparticles have commercial and industrial applications including use in pigments,[4] catalysts,[5] adsorbents,[6] magnetic materials,[7] and sensors.[8] Numerous chemical synthetic routes for the production of nano-scale iron oxide particles are available including microemulsion formation, sol–gel syntheses, sonochemical reactions, hydrothermal reactions, hydrolysis and thermolysis of precursor particles, flow injection and electrospray.[9,10]

Fine control of the phase and size of iron-oxide-based nanoparticles has been demonstrated in organic solvent-based syntheses. Examples include selected iron oxide phase nanoparticles prepared from $Fe(CO)_5$ precursors in a variety of organic solvents with a relatively uniform particle size range.[11,12] DeCaro *et al.*[13] among them also reported on a relation between particle size and the phase structure of the particle. The stability of iron oxide nanoparticles was demonstrated in the work by Insin *et al.*,[14] who immobilized iron-oxide particles onto silica microspheres for sufficient periods to perform fluorescence imaging. Tuneability of the sizes of particles made from other metals was demonstrated by the work of Weller *et al.*, who used temperature and stabilizing agents to control the size of biphasic Pt–Fe or Pt–Co particles.[15,16] However, a drawback to these and many similar sol–gel synthetic approaches is the need for organic solvents, a feature that can deter industrial adoption for environmental and cost reasons. Thus, we have explored an approach for nano-scale particle formation that minimizes or excludes the use of organic solvents.

One common and simple method for iron-oxide particle formation that avoids the use of organic solvents is hydrolysis.[17–19] Unfortunately, existing synthesis techniques have shown poor control over the particle size and chemical composition of the final product. The chemical phase of the product has been found to be highly sensitive to the reaction conditions (*e.g.*, solution pH), the concentration of iron species, and the polarity of the solution. Also, a range of oxides (often as a mixture of oxides of different phases) are created. The oxides found in a final product(s) include ferrihydrite ($Fe_5HO_8{\cdot}4H_2O$), goethite (α-FeOOH), akagenite (β-FeOOH), lepidocrocite (γ-FeOOH), maghemite (γ-Fe_2O_3), hematite (α-Fe_2O_3), and magnetite (Fe_3O_4).[19–23]

Generation of a pure, single-phase particulate product remains a challenge, especially *via* a synthetic route that can be easily adopted to produce a particular specific ferric chemical species without using organic solvents. In this paper, we describe a method for synthesizing single-phase iron oxyhydroxide (α- and γ-FeOOH) nanoparticles using forced hydrolysis of an aqueous ferric nitrate solution. In addition, the γ-FeOOH particles that we have produced can be subsequently thermally treated to convert them to other single-phase iron-oxide/hydroxide nanoparticles. The main objective of this research is not synthesis per se, but rather, developing an understanding

[a] *Department of Chemistry, The University of Western Ontario, London, Ontario, Canada N6A 5B7*
[b] *Department of Mechanical and Materials Engineering, The University of Western Ontario, London, Ontario, Canada N6A 5B7. E-mail: jcwren@uwo.ca; Fax: +1 519 661 3022; Tel: +1 519 661 2111x86339*

of underlying physical and chemical properties that determine the size and phase of nanoparticles. To this end, a dependence of the phase of FeOOH produced on the initial solution ferric concentration has led us to propose potential growth mechanisms that differentiate the production of the α- and γ-FeOOH phases.

2. Experimental

Solutions were prepared containing various concentrations (0.01–0.05 M) of $Fe(NO_3)_3$ (Sigma, analytical grade) dissolved in water purified and de-ionized with a NANOpure Diamond UV ultrapure water system (Barnstead International) to a resistivity of 18.2 MΩ cm. These solutions were placed in open beakers and heated to, and held at, 60 °C for 24 h. This heating period was previously found to be optimum for depositing single-phase γ-FeOOH films on glass surfaces.[24] After heating for ~10 h, the solution became visibly cloudy, and at longer times yellow or orange precipitates appeared at the bottom of the beakers. No further precipitation was observed after 24 h. After heating, the contents of the beaker were centrifuged to collect the fine yellow or orange (depending on the $Fe(NO_3)_3$ concentration) precipitates. Samples of this material were transferred to watch glasses and air dried prior to characterization by X-ray diffraction (XRD), FT-IR and transmission electron microscopy (TEM). To ensure reproducibility, multiple trials of these experiments were performed, and products were analyzed using XRD.

The XRD analysis was performed using a Rigaku RTP 300RC diffractometer with Cu-Kα radiation. The particle sizes were calculated based on the measured Scherrer broadening of the XRD peaks, as described in Section 20 of ref. 25. The FT-IR spectroscopy was performed using a Bruker Vertex 70V FT-IR Spectrometer. For the FT-IR analyses, the particulate samples and the standards of mineral iron oxyhydroxide powders (purchased from Alfa Aesar) were dispersed in KBr powder and this mixture was pressed into a pellet for analysis. The spectra were integrated over 64 individual scans. The FT-IR analysis provides a qualitative determination of the chemical nature of the sample particulate; no attempt was made to use the FT-IR analyses for quantitative analysis. TEM was performed using a Philips EM 410 electron microscope and the particle sizes were determined directly from the resulting images.

As discussed in the results section below, the particulate formed by hydrolysis of a low concentration $Fe(NO_3)_3$ solution was found to be relatively pure γ-FeOOH. Samples of this particulate, after collection by centrifuging and drying, were further treated to change the particulate chemical composition and phase. Three additional processing routes were tested starting with the pure γ-FeOOH (illustrated in Fig. 1). For route 1 (to form α-Fe_2O_3), a sample of the γ-FeOOH particulate was transferred to a crucible, placed in an oven and calcined at a temperature of 400 °C in air for 2 h. For route 2, the γ-FeOOH particulate was allowed to react in an aqueous solution containing 0.01 M $FeSO_4$ and 0.4 M sodium acetate at 60 °C. The particulate was then collected by centrifuging and drying in a manner similar to that used to collect the initial γ-FeOOH. This route leads to formation of Fe_3O_4. For route 3,

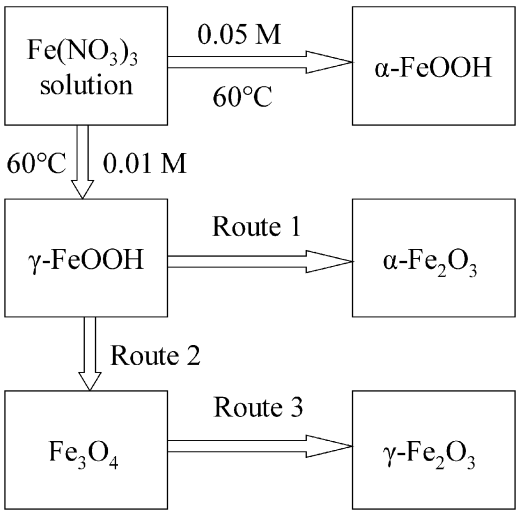

Fig. 1 Schematic of the production processes for various iron oxyhydroxides and oxides from hydrolysis of $Fe(NO_3)_3$.

the particulate produced by following route 2 was calcined in a manner similar to that used in route 1, except that the temperature was held at 250 °C for one hour. This leads to formation of γ-Fe_2O_3.

The particulates collected at the end of these three processing routes were examined using the same TEM and XRD techniques used to analyze the initially-produced γ-FeOOH particulate.

3. Results

3.1 Formation of γ-FeOOH and α-FeOOH nanoparticles

Fig. 2 presents the XRD patterns observed for the particulates formed in $Fe(NO_3)_3$ solutions of different concentrations. At the lowest concentration studied (0.01 M), the product composition was predominantly γ-FeOOH (line a), whereas at the highest concentration, 0.05 M, it was predominantly α-FeOOH (line i). Mixtures of γ- and α-FeOOH were obtained

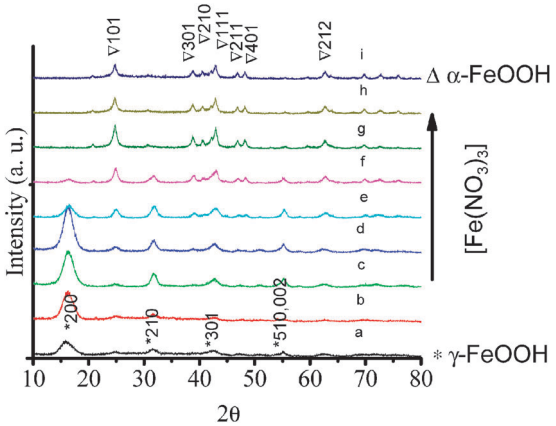

Fig. 2 XRD patterns of the products obtained after 24 h hydrolysis of various $Fe(NO_3)_3$ concentration solutions at 60 °C: (a) 0.01, (b) 0.015, (c) 0.02, (d) 0.025, (e) 0.03, (f) 0.035, (g) 0.04, (h) 0.45 and (i) 0.05 M. The main 2θ peaks for γ-FeOOH are denoted by * and those of α-FeOOH by Δ.

when the $Fe(NO_3)_3$ concentration was between 0.015 and 0.04 M (lines b–h). The XRD patterns show that as the $Fe(NO_3)_3$ concentration increases from 0.01 M, peaks at 2θ values of 24.7° and 62.6° that correspond to the α-FeOOH phase grow, and the γ-FeOOH phase peaks at 2θ values of 15.8°, 31.5°, 42.6° and 55.1° diminish. For $Fe(NO_3)_3$ concentrations greater than 0.035 M, α-FeOOH becomes the dominant phase produced and at concentrations above 0.04 M (lines h and i of Fig. 2) only α-FeOOH peaks were detected.

The visual appearance of the hydrolysis products changes to match the change in the dominant phase formed. The particulate material collected from the 0.01 M solution was orange while that collected from the 0.05 M solution was yellow; these are the accepted colours of γ-FeOOH and α-FeOOH respectively.[23] While the visual inspection is consistent with the production of two different, relatively pure phases at the low and high ends of the tested solution concentrations, there are limits on the purity that can be established using the XRD analysis. Various XRD detection limits have been quoted for iron oxides; 0.2 wt%[25] or in a range of 0.1–0.5 wt%.[26] Based on these, it is reasonable to suggest that minor phases in the 'pure' γ-FeOOH and α-FeOOH particulates produced in our syntheses do not exceed 1 wt%.

The Scherrer peak broadening of the γ-FeOOH XRD patterns in Fig. 2 can be used to determine the nominal sizes of the particle produced.[25] The width of the peak at 2θ = 17° (corresponding to γ-FeOOH, and indicated by the notation "200" in Fig. 2) was used to obtain the sizes of the particulates produced from solutions with different concentrations (lines a to e in Fig. 2). The particle sizes determined by this method are presented in Fig. 3. The results show an increase in nominal particle size from 4 to 5 nm as the $Fe(NO_3)_3$ concentration increased from 0.01 to 0.03 M. Similarly, the sizes of α-FeOOH particles shown in Fig. 3 were calculated from the peak at 2θ = 25° (denoted by "101" in Fig. 2). The α-FeOOH particle size has a roughly linear dependence on the $Fe(NO_3)_3$ concentration over the studied range of 0.025–0.05 M, increasing from 5 to 15 nm. This indicates that it is possible to fabricate particles to a desired (average) size, simply by adjusting the $Fe(NO_3)_3$ concentration used in the synthesis.

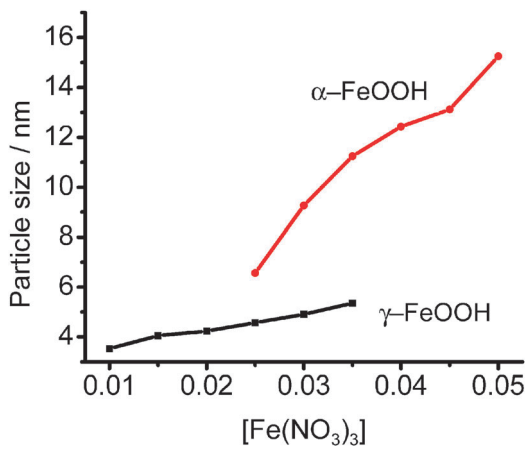

Fig. 3 Particle size as a function of $Fe(NO_3)_3$ concentration for α-FeOOH (●) and γ-FeOOH (■).

Fig. 4 shows the FT-IR spectra of the hydrolysis products formed in different $Fe(NO_3)_3$ concentration solutions. All samples have two broad bands at 3200 and 3400 cm^{-1} that can be attributed to the vibrational stretch mode of bulk and surface O–H, respectively[27–29] (found in both FeOOH compounds). All of the samples have a very narrow peak at *ca.* 1380 cm^{-1} that can be attributed to residual nitrate ions adsorbed on the samples.[30,31] At the lowest concentration studied (0.01 M), a low intensity peak appears at 1020 cm^{-1} that corresponds to the δ_{OH} in-plane bending mode for γ-FeOOH.[29,32] This peak is critical in determining the sample concentration of γ-FeOOH as it diminishes with increasing $Fe(NO_3)_3$ solution concentration, disappearing when the $Fe(NO_3)_3$ concentration reaches 0.04 M. When the $Fe(NO_3)_3$ solution concentration reaches 0.035 M, two new peaks appear at 801 and 888 cm^{-1}. These peaks can be attributed to δ_{OH} in-plane bending and γ_{OH} out-of-plane bending for α-FeOOH.[27,32] An additional peak appears for α-FeOOH Fe–O symmetric stretch at 614 cm^{-1}, which indicates well-defined crystallinity for the α-FeOOH formed at high $Fe(NO_3)_3$ solution concentrations.[29]

Fig. 5 shows the TEM images of the γ-FeOOH and α-FeOOH particles formed at $Fe(NO_3)_3$ concentrations of 0.01 and 0.05 M, respectively. The large aggregate shown in Fig. 5a is an agglomeration of the precipitate of the γ-FeOOH particles formed in a 0.01 M $Fe(NO_3)_3$ solution and has an irregular amorphous shape. This aggregate is comprised of crystallites of approximately 4 nm in diameter as can be seen in the high-magnification image in Fig. 5b. The precipitates of α-FeOOH formed in a 0.05 M $Fe(NO_3)_3$ solution agglomerate into much larger spherical particles, ~100 nm in diameter, Fig. 5c, and these aggregates are comprised of crystallites with a rod shape and a

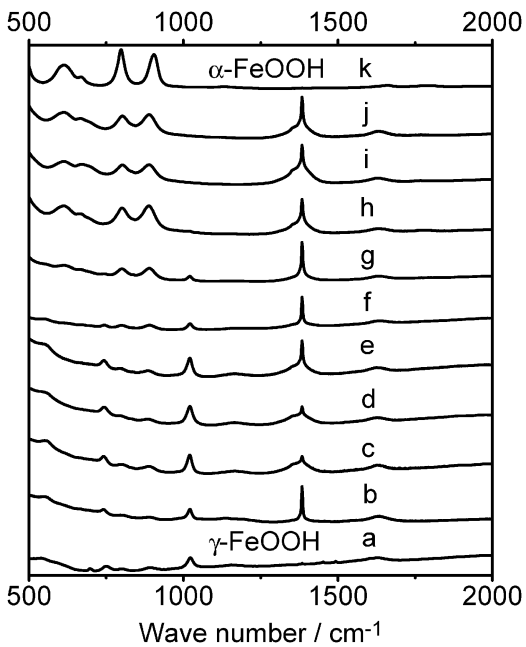

Fig. 4 FT-IR spectroscopy of the products obtained after 24 h hydrolysis of various $Fe(NO_3)_3$ concentration solutions at 60 °C: (a) standard γ-FeOOH, (b) 0.01, (c) 0.015, (d) 0.02, (e) 0.025, (f) 0.03, (g) 0.035, (h) 0.04, (i) 0.45, (j) 0.05 M $Fe(NO_3)_3$ and (k) standard α-FeOOH.

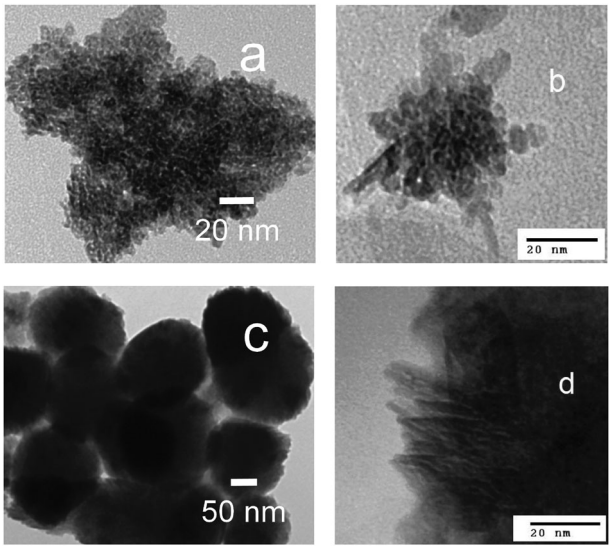

Fig. 5 TEM images of (a) and (b) γ-FeOOH; and (c) and (d) α-FeOOH nanoparticles.

length of approximately 10 nm, Fig. 5d. The sizes of the small γ-FeOOH and α-FeOOH particles that form the larger aggregates observed in TEM images are consistent with the particle sizes determined from the XRD peak broadening, Fig. 2.

No insoluble substances were observed at higher concentrations (>0.05 M) of $Fe(NO)_3$ and only clear yellow solutions were obtained. At these high concentrations, the pH of the ferric nitrate solution is very low (<1.5) and at these pHs the change in the hydrolysis equilibrium in heating the solutions from room temperature to 60 °C is not sufficient to shift the equilibrium to form iron oxyhydroxide particles.

3.2 Conversion of γ-FeOOH to other iron oxides

As described in the experimental section, γ-FeOOH can be easily transformed to α-Fe_2O_3, γ-Fe_2O_3 and Fe_3O_4 by the processing routes illustrated in Fig. 1. The materials formed are pure-phase α-Fe_2O_3, Fe_3O_4 and γ-Fe_2O_3 as determined by XRD, as shown in Fig. 6. The XRD patterns shown in Fig. 6 match the known patterns of these species. No significant impurity peaks were observed in the XRD patterns indicating complete transformation of the initial species; again we set a limit on purity to mean less than 1 wt% of material of another phase. Calcining γ-FeOOH with a particle size of ~4 nm at 400 °C (route 1 in Fig. 1) produces α-Fe_2O_3 with a particle size of 16 nm (as derived from the width of the "104" XRD peak in Fig. 6). Similarly, fabrication route 2 (in Fig. 1) produces Fe_3O_4 with a particle size of 22 nm (as derived from the width of "220" XRD peak in Fig. 6). The Fe_3O_4 has a much larger size than the γ-FeOOH precursor particle size. Previous studies suggest that in route 2 the particle phase transformation proceeds *via in situ* dehydration and local rearrangement.[21,33,34] However, such a transformation may also occur *via* dissolution-crystallization initiated by surface adsorption of Fe(II), a mechanism that has been used to explain the electro-reduction and oxidation kinetics of H_2O_2 on single-phase γ-FeOOH films on indium tin oxide glasses.[35] Regardless of the mechanism, calcination of the Fe_3O_4 particles at 250 °C leads to

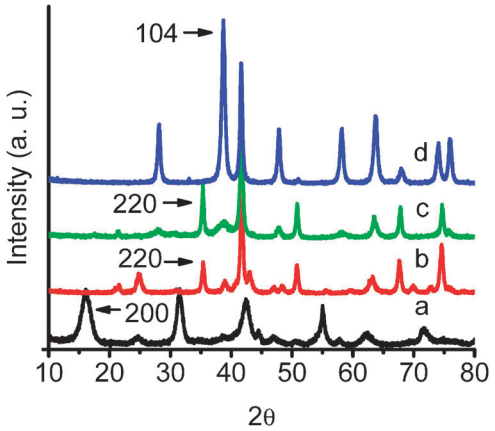

Fig. 6 XRD patterns for (a) γ-FeOOH obtained from the hydrolysis of a 0.01 M $Fe(NO_3)_3$ solution, (b) Fe_3O_4 formed by reacting γ-FeOOH with Fe^{2+}, (c) γ-Fe_2O_3 formed by calcining Fe_3O_4 at 250 °C, and (d) α-Fe_2O_3 formed by calcining γ-FeOOH at 400 °C.

further transformation to γ-Fe_2O_3 with an even larger particle size of 29 nm. This is ~30% larger than the size of the Fe_3O_4 precursor particles and this increase is attributed to a growth of the iron-oxide crystals that make up the particles since additional oxygen is incorporated in the crystal lattice to transform Fe_3O_4 to γ-Fe_2O_3. The morphologies of the α-Fe_2O_3, Fe_3O_4 and γ-Fe_2O_3 particles were examined by TEM, Fig. 7. In the TEM images, the black spherical shapes are iron oxide particles; the translucent rod shapes or sheets are broken carbon films from TEM grids, and are not iron-oxide crystallites.

4. Discussion

Targeted production of pure iron oxyhydroxides as a well-defined, fine particulate opens opportunities for the use of these materials. In general, it is difficult to develop such a targeted production process because it is hard to predict which oxide phase will form under a given set of conditions. The main reason for this is that the stabilities of the different iron oxyhydroxides and transformation between different phases in the synthetic processes are not well understood. An underlying issue is a lack of knowledge of the structural details, thermodynamic properties, and reactivity of individual iron oxides as the synthesis proceeds and particles nucleate and grow.[36] Smaller particles, in general, have higher enthalpies and free energies of formation than larger crystals because they have more positive surface energy.[36] In water, the particle surfaces are also hydrated and, thus, the growth of the particles will depend on the thermodynamics of species in the bulk phase,

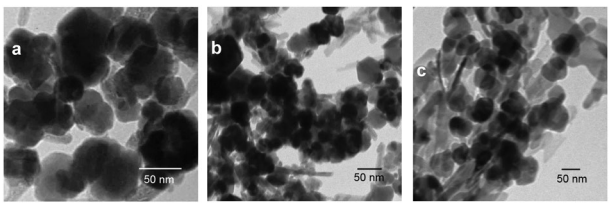

Fig. 7 TEM images of (a) α-Fe_2O_3, (b) Fe_3O_4, and (c) γ-Fe_2O_3 nanoparticles.

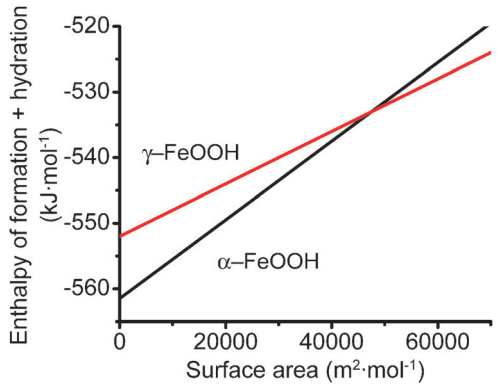

Fig. 8 The sum of the enthalpies of bulk-phase formation and surface hydration for α-FeOOH and γ-FeOOH as a function of surface area.

the particle size (or surface area), and the extent of hydration.[36] The enthalpies of formation for α-FeOOH and γ-FeOOH are -561.5 ± 1.5 kJ mol^{-1} and -552.0 ± 1.6 kJ mol^{-1}, respectively.[37,38] Hence, solid α-FeOOH is thermodynamically more stable and would be expected to form preferentially. However, the surface enthalpies for hydration on α-FeOOH and γ-FeOOH are 0.60 ± 0.10 J m^{-2} and 0.40 ± 0.16 J m^{-2}, respectively.[36–38] As a consequence, hydration increases the thermodynamic stability of γ-FeOOH–H_2O compared to α-FeOOH–H_2O.

The combined effect of these two thermodynamic factors is shown in Fig. 8, which plots the sum of the enthalpies of formation and surface hydration as a function of surface area for α-FeOOH and γ-FeOOH at room temperature. This plot is normalized for the mass of the material. Fig. 8 shows that α-FeOOH is more thermodynamically stable when present as large particles (with low specific surface areas) while γ-FeOOH is more stable when present as small particles. The transition point is at a specific surface area of 4.72×10^4 m^2 mol^{-1} or 530 m^2 g^{-1}. This value corresponds to a 3 nm particle size, assuming a spherical particle shape. Non-spherical particles would have higher surface areas to mass ratios than spherical particles and favour the γ-FeOOH phase for even larger nominal particle sizes. Unfortunately, the exact dependence on particle shape cannot be fully explored at this time as thermodynamic data for hydrolysis on individual crystal planes are not available. In this work we have used average enthalpy values for surface hydration and anisotropies of the particles and the effects of anisotropy have been ignored. Allowing for this simplification, the cross-over point for particle stability is in good agreement with our experimental observation that γ-FeOOH is formed as the dominant phase in particles with a size in the range of 4 to 5 nanometers. Furthermore this observation is consistent with formation of only γ-FeOOH in solutions where the concentration of iron is low and there is insufficient material to produce larger-sized particles. The stable species becomes α-FeOOH when the particle size exceeds 6 nm (Fig. 3).

Thermodynamics favour the formation of γ-FeOOH particles at the earliest stages of particle growth when the particles are extremely small. However, the process by which this initial particle nucleation occurs and the subsequent mechanism of growth to nanometer scale is still not clear. In particular, why do individual particles of γ-FeOOH, once formed, convert to α-FeOOH particles, simply because bulk thermodynamics favours the α phase for a larger particle? Two potential mechanisms for crystal growth can explain our observations; both are related to the density of Fe^{3+} ions in solution.[39] In both mechanisms the final phase of the iron oxyhydroxide is related to the rate of particle growth following nucleation.

For both mechanisms, the initial nucleation is achieved by the hydration of Fe^{3+} ions, followed by poly-condensation/dehydration to form amorphous ferric-hydroxide ($Fe(OH)_3$) particles:[40]

$$Fe^{3+}(aq) \leftrightarrows Fe(H_2O)_{6-n}(OH)_n^{(3-n)}(aq) \quad (1a)$$

$$Fe(H_2O)_3(OH)_3(aq) \rightarrow Fe(OH)_3(s) \quad (1b)$$

where $Fe(H_2O)_{6-n}(OH)_n^{(3-n)}$ represents all of the hydrated ferric species including $Fe(H_2O)_3(OH)_3(aq)$ that are in acid–base equilibrium with each other, with n ranging from 1 to 4, and (aq) and (s) represent aqueous and solid phases, respectively. The primary $Fe(OH)_3(s)$ particles provide nucleation sites where Fe^{III} ions can further condense and the iron oxide particles can grow outward. This nucleation step is assumed to occur relatively fast in both mechanisms.

Following nucleation, the subsequent growth of specific phases of oxyhydroxide particles can occur *via* two ways. In the first mechanism, the ferric ions can continually condense as $Fe(OH)_3(s)$ on the nucleates. These primary $Fe(OH)_3$ particles grow to a specific size depending on the ferric nitrate concentration in solution. They then slowly undergo further dehydration or phase transition to form γ-FeOOH or α-FeOOH. In dilute solutions with few Fe^{3+} ions available, only very small $Fe(OH)_3$ particles can be grown by this mechanism, thus favouring subsequent phase transition to γ-FeOOH. Conversely, larger $Fe(OH)_3$ particles could be formed in more concentrated solutions, favouring the phase transition to larger α-FeOOH particles. At intermediate solution concentrations, mixtures of the two phases would be produced. Fig. 9 shows a schematic of this mechanism.

In the second proposed mechanism, Fig. 10, the ferric ions also deposit on the $Fe(OH)_3$ nucleates but the particles transform into a specific oxyhydroxide phase as they grow rather than by a phase transformation of the $Fe(OH)_3$ particles. The phase of iron oxide/hydroxide crystals grown in this way will depend on the surface energy of the crystal particle, which changes as the particle grows.[41,42] Hence, the resulting phase will be particularly sensitive to the ionic strength of the solution. Increasing the concentration of the starting $Fe(NO_3)_3$ solution will increase both the ionic strength and the ferric ion concentration and together these two factors will determine the ferric ion solvation (or hydration) stabilities. The change in the energy of hydration for the two different species could account for the shift to α-FeOOH formation at higher $Fe(NO_3)_3$ concentrations. This particle growth mechanism can also explain the different crystal shapes observed for γ-FeOOH (spherical) and α-FeOOH (rod shape) particles.[43]

An additional important parameter for the hydrolysis and phase stability of the iron oxyhydroxides is pH. In these experiments, the initial pH of the solution was low (measured to be pH 1.5 in 0.05 M $Fe(NO_3)_3$ solutions). During the hydrolysis, the

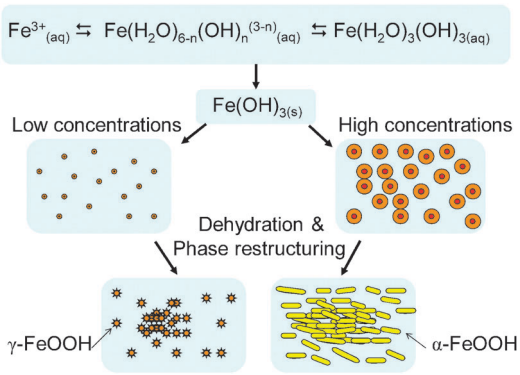

Fig. 9 Schematic of proposed growth **mechanism 1**: Fast formation of the $Fe(OH)_{3(s)}$ nucleates, followed by growth of $Fe(OH)_{3(s)}$, and then by dehydration and phase restructuring to form specific-phase oxyhydroxides.

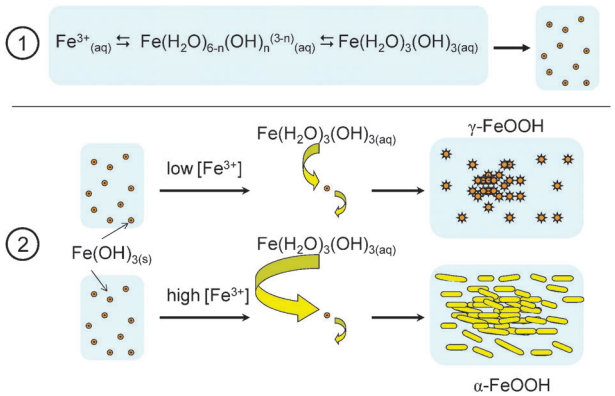

Fig. 10 Schematic of proposed growth **mechanism 2**: Fast formation of the $Fe(OH)_{3(s)}$ nucleates, followed by the deposition Fe^{III} ions on the $Fe(OH)_3$ nucleates and then by solid-state growth into specific-phase oxyhydroxides.

pH increased to pH 2.5. Although Fe^{3+} hydration increases the H^+ concentration, even the complete hydration of 0.05 M Fe^{3+} (our most concentrated solution) can not affect the pH too much due to the initial pH. While pH is an important parameter for the phase stability of iron oxide/hydroxide, the first acidity constants, pK_{a1}, for lepidocrocite and goethite are both greater than 4 [23]. Hence, over the pH range of 1.5 to 2.5 the stabilities of lepidocrocite and goethite should be similar. In addition, the phase conversion of $Fe(H_2O)_3(OH)_3(aq)$ to $Fe(OH)_3(s)$ is expected to be slower than the hydrolysis equilibria of reaction (1a), and further irreversible conversion rate for $Fe(OH)_3(s)$ to γ-FeOOH or α-FeOOH should be less sensitive to pH. While the change in pH that occurred during our experiments may impact on the kinetics of formation of the $Fe(OH)_3(s)$ particle nucleates, it will not change the overall reaction direction.

At this time, there is no concrete experimental evidence that can unequivocally support either mechanism, although we prefer the second mechanism since it can also explain the observed dependence of crystal shape on oxyhydroxide phase. Both α-FeOOH and γ-FeOOH have an orthorhombic, bipyramidal unit cell, but the goethite structure consists of an hcp (hexagonal close packed) array of anions (O^{2-}/OH^-) stacked along the "010" direction with Fe^{III} occupying half the octahedral interstices within a layer, while the structure of lepidocrocite consists of ccp (cubic close packed) anions stacked along the "150" direction with Fe^{III} occupying the octahedral.interstices [23]. Goethite thus has a tunnel structure, whereas lepidocrocite is a layered compound. It has also been reported that the goethite structure bonding is weakest along the "010" direction because the hydrogen bonding between the double chains of the octahedra have the strongest vector in this direction [23]. Therefore, it is reasonable to assume that α-FeOOH would grow preferentially in the direction perpendicular to the "010" plane. This preferential growth is expected to be more pronounced under conditions such as ours, in which the internal defects cannot be improved by stirring or heating. For α-FeOOH, the naturally grown mineral goethite typically has a rod or needle-like shape. This suggests that α-FeOOH prefers to grow on one particular plane. Under our synthesis conditions, there appears to be no preferential growth on any crystal plane of γ-FeOOH. This may be due to the very small size of the particles of γ-FeOOH being formed. Additionally, it is also possible that the differences in the hydrogen bonding structure of the two oxyhydroxides lead to crystal growth in different directions. Although all of the hydrogen bonds are structurally equivalent in each FeOOH, they point in two different directions in goethite whereas they point in only one direction in lepidocrocite [23]. The hydrogen bonding in lepidocrocite is less directional, leading to less preferential growth in a specific direction.

A more complete understanding of the basis for the selectivity of the FeOOH production is a subject for further study. Whatever the exact mechanism is, this study shows that the solution concentration of ferric ions is an important parameter in determining the phase and the size of ferric oxyhydoxide nanoparticles that can be formed. The α-FeOOH or γ-FeOOH particles grow until the system reaches a phase equilibrium dictated by thermodynamics, as discussed above. The primary FeOOH particles aggregate into larger particles and the mechanism for this aggregation also strongly depends on surface energy and, hence, crystal shape and ionic strength. Aggregation mechanisms have been studied by other groups[41,44–47] and are beyond the scope of this work.

5. Conclusion

Nanoparticles of single-phase lepidocrocite (γ-FeOOH) and goethite (α-FeOOH) have been synthesized by forced hydrolysis of ferric nitrate in warm (60 °C) water without any other additives. At low $Fe(NO_3)_3$ concentrations, the hydrolysis product is predominantly γ-FeOOH, while at higher concentrations it is α-FeOOH. The particles produced are nanometer sized with narrow size distributions. The relationship between the oxyhydoxide phase and the particle size formed is attributed to the influence of two thermodynamic factors, the enthalpy of formation and the surface enthalpy of hydration at the oxide-water interface as a function of surface area. It is proposed that a shift in hydrolysis equilibrium as temperature increases (from room temperature to 60 °C) causes $Fe(OH)_3$ to form nucleation condensates which then grow into a specific FeOOH phase depending on the solution ferric ion concentration. Two potential mechanisms for the formation of FeOOH

particles with a specific phase are proposed that can explain the dependency of the phase type on the Fe^{3+} solution concentration. The γ-FeOOH nanoparticles were converted to larger α-Fe_2O_3, Fe_3O_4 and γ-Fe_2O_3 particles by simple thermal/chemical treatments. These simple controlled syntheses of iron oxide particles with well-controlled characteristics have potential applications in laboratory, industrial, and environmental processes.

Acknowledgements

The funding from the Canadian Natural Science and Engineering Research Council (NSERC) Discovery grant is greatly acknowledged. The authors wish to thank Ms Grace C. Yau of the Department of Earth Science for the X-ray diffraction measurements and Ms Judith E. Sholdice of the Department of Microbiology and Immunology for assistance in transmission electron microscope photography.

References

1 X. Wang, J. Zhuang, Q. Peng and Y. D. Li, *Nature*, 2005, **437**, 121–124.
2 *Nanoscale Materials in Chemistry*, ed. K. J. Klabunde and R. M. Richards, John Wiley & Sons Inc., New York, 2001.
3 *The Chemistry of Nanomaterials: Synthesis, Properties and Applications*, ed. C. N. R. Rao, A. Muller and A. K. Cheetham, Wiley-VCH, Weinheim, Weinheim, Germany, 2004.
4 *The Iron Oxide: Structure, Properties, Reactions, Occurrence and Uses*, ed. R. M. Cornell and U. Schwertmann, VCH, Weinheim, 1996.
5 M. Hermanek, R. Zboril, N. Medrik, J. Pechousek and C. Gregor, *J. Am. Chem. Soc.*, 2007, **129**, 10929–10936.
6 O. K. Hartzog, V. A. Loganathan, S. R. Kanel, G. R. Jeppu and M. O. Barnett, *J. Colloid Interface Sci.*, 2009, **333**, 6–13.
7 P. Majewski and B. Thierry, *Crit. Rev. Solid State Mat. Sci.*, 2007, **32**, 203–215.
8 L. Stanciu, Y. H. Won, M. Ganesana and S. Andreescu, *Sensors*, 2009, **9**, 2976–2999.
9 S. Laurent, D. Forge, M. Port, A. Roch, C. Robic, L. V. Elst and R. N. Muller, *Chem. Rev.*, 2008, **108**, 2064–2110.
10 A. S. Teja and P.-Y. Koha, *Prog. Cryst. Growth Charact. Mater.*, 2009, **55**, 22.
11 X. W. Teng and H. Yang, *J. Mater. Chem.*, 2004, **14**, 774–779.
12 K. Woo, J. Hong, S. Choi, H. W. Lee, J. P. Ahn, C. S. Kim and S. W. Lee, *Chem. Mater.*, 2004, **16**, 2814–2818.
13 D. deCaro, T. O. Ely, A. Mari, B. Chaudret, E. Snoeck, M. Respaud, J. M. Broto and A. Fert, *Chem. Mater.*, 1996, **8**, 1987–1991.
14 N. Insin, J. B. Tracy, H. Lee, J. P. Zimmer, R. M. Westervelt and M. G. Bawendi, *ACS Nano*, 2008, **2**, 197–202.
15 S. H. Sun, C. B. Murray, D. Weller, L. Folks and A. Moser, *Science*, 2000, **287**, 1989–1992.
16 E. V. Shevchenko, D. V. Talapin, H. Schnablegger, A. Kornowski, O. Festin, P. Svedlindh, M. Haase and H. Weller, *J. Am. Chem. Soc.*, 2003, **125**, 9090–9101.
17 N. Pailhe, J. Majimel, S. Pechev, P. Gravereau, M. Gaudon and A. Demourgues, *J. Phys. Chem. C*, 2008, **112**, 19217–19223.
18 M. Schultz, W. Burckhardt and S. Barth, *J. Mater. Sci.*, 1999, **34**, 2217–2227.
19 W. Wang, J. Y. Howe and B. H. Gu, *J. Phys. Chem. C*, 2008, **112**, 9203–9208.
20 M. Gotić, S. Popović, N. Ljubešić and S. Musić, *J. Mater. Sci.*, 1994, **29**, 2474–2480.
21 X. Liang, X. Wang, J. Zhuang, Y. T. Chen, D. S. Wang and Y. D. Li, *Adv. Funct. Mater.*, 2006, **16**, 1805–1813.
22 M. Loan, O. G. M. Newman, J. B. Farrow and G. M. Parkinson, *Cryst. Growth Des.*, 2008, **8**, 1384–1389.
23 *Iron Oxides in the Laboratory: Preparation and Characterization*, ed. U. Schwertmann and R. M. Cornell, Wiley-VCH, 2nd, Completely Revised and Enlarged Edition, 2001.
24 D. Fu and J. C. Wren, *J. Nucl. Mater.*, 2008, **374**, 116.
25 *Industrial Applications of X-Ray Diffraction*, ed. F. H. Chung and D. K. Smith, Marcel Dekker Inc., 1999.
26 C. Linke, O. Mohler, A. Veres, A. Mohacsi, Z. Bozoki, G. Szabo and M. Schnaiter, *Atmos. Chem. Phys.*, 2006, **6**, 3315–3323.
27 P. Cambier, *Clay Miner.*, 1986, **21**, 191–200.
28 P. Cambier, *Clay Miner.*, 1986, **21**, 10.
29 D. G. Lewis and V. C. Farmer, *Clay Miner.*, 1986, **21**, 93–100.
30 S. Bashir, R. W. McCabe, C. Boxall, M. S. Leaver and D. Mobbs, *J. Nanopart. Res.*, 2008, **11**, 701–706.
31 C. J. Mena-Duran, M. R. S. Kou, T. Lopez, J. A. Azamar-Barrios, D. H. Aguilar, M. I. Dominguez, J. A. Odriozola and P. Quintana, *Appl. Surf. Sci.*, 2007, **253**, 5762–5766.
32 A. Bewick, M. Kalaji and G. Larramona, *J. Electroanal. Chem.*, 1991, **318**, 207–221.
33 J. P. Jolivet, C. Chaneac and E. Tronc, *Chem. Commun.*, 2004, 481–487.
34 M. J. Meziani, P. Liu, P. Pathak, J. Lin, S. K. Vajandar, L. F. Allard and Y.-P. Sun, *Ind. Eng. Chem. Res.*, 2006, **45**, 1539–1541.
35 D. Fu, X. Zhang, P. G. Keech, D. W. Shoesmith and J. C. Wren, *Electrochim. Acta*, 2010, **55**, 3787–3796.
36 A. Navrotsky, L. Mazeina and J. Majzlan, *Science*, 2008, **319**, 1635–1638.
37 J. Majzlan, L. Mazeina and A. Navrotsky, *Geochim. Cosmochim. Acta*, 2007, **71**, 615–623.
38 L. Mazeina and A. Navrotsky, *Clays Clay Miner.*, 2005, **53**, 113–122.
39 C. M. Flynn, *Chem. Rev.*, 1984, **84**, 31–41.
40 A. Stefansson, *Environ. Sci. Technol.*, 2007, **41**, 6117–6123.
41 J. G. Hockridge, F. Jones, M. Loan and W. R. Richmond, *J. Cryst. Growth*, 2009, **311**, 3876–3882.
42 P. C. Rieke, B. D. Marsh, L. L. Wood, B. J. Tarasevich, J. Liu, L. Song and G. E. Fryxell, *Langmuir*, 1995, **11**, 318–326.
43 S. Krehula and S. Music, *J. Cryst. Growth*, 2008, **310**, 513–520.
44 R. L. Penn, J. J. Erbs and D. M. Gulliver, *J. Cryst. Growth*, 2006, **293**, 1–4.
45 G. A. Waychunas, C. S. Kim and J. F. Banfield, *J. Nanopart. Res.*, 2005, **7**, 409–433.
46 J. Rose, A. Manceau, J. Y. Bottero, A. Masion and F. Garcia, *Langmuir*, 1996, **12**, 6701–6707.
47 M. Zic, M. Ristic and S. Music, *Mater. Chem. Phys.*, 2010, **120**, 160–166.